Local Tracing of Curvilinear Structures in Volumetric Color Images: application to the Brainbow analysis

E. Bas[a,*], D. Erdogmus[a], R.W. Draft[b], J.W. Lichtman[b]

[a] *Department of Electrical and Computer Engineering, Northeastern University, 360 Huntington Ave., 409 Dana Research Center, Boston, MA, 02148*
[b] *Department of Molecular and Cellular Biology and Center for Brain Science, Harvard University, Cambridge, Massachusetts 02138*

Abstract

In this study, we compare two vectorial tracing methods for 3D color images: (i) a conventional piecewise linear generalized cylinder algorithm that uses color and edge information and (ii) a principal curve tracing algorithm that uses the gradient and Hessian of a given density estimate. We tested the algorithms on synthetic and Brainbow dataset to show the effectiveness of the proposed algorithms. Results indicate that the proposed methods can successfully trace multiple axons in dense neighborhoods.

Keywords: volumetric color images, piecewise linear cylinder model, principal curve, Brainbow, axon tracing, connectivity analysis, topological skeleton

1. Introduction

It is impossible to throughly understand the function of a complex system without understanding its basic elements. For that reason morphology (geometry and topology) of neurons is of broad interest, in order to comprehend the function and connectivity of neurons as well as to detect miswiring as may occur in Alzheimer's and Parkinson's diseases (Kasthuri and Lichtman, 2003; Feng et al., 2000). Various imaging techniques have been utilized to uncover morphology. Resolution limitations in optical imaging, problems related to sample preparation and most dominantly, the diversity and the complexity of neuronal arbors are some of the major challenges in neuroinformatics. With recent improvements in 3D imagery techniques, high volumes of data are available as image stacks, but obtained images are not always discriminative and conclusive. Hence, they require tedious and, most of the time, impractical manual processing. Therefore, reliable and efficient techniques are needed to process

*Corresponding author
Email addresses: bas@ece.neu.edu (E. Bas), erdogmus@ece.neu.edu (D. Erdogmus), draft@fas.harvard.edu (R.W. Draft), jeff@mcb.harvard.edu (J.W. Lichtman)

these data with minimum initialization/parametrization and easy user intervention.

Significant research effort has been dedicated to the segmentation and analysis of curvilinear objects that arise in various contexts (e.g. vascular networks, bronchia) (Sato et al., 1998; Aykac et al., 2003; Nain et al., 2004; Cruz et al., 2004; Zhou et al., 2008). In general, segmentation is the first step to outline an object. Further analysis is needed to extract the topology information from the segmented image stack, which ranges from unsupervised skeletonization techniques to model based approaches. A recent literature review for the analysis of linear branched structures can be found easily (Meijering, 2010). However, it is safe to claim that all tree extraction methods in the literature seek the underlying ridge (trace) of the curvilinear structure.

Definition of a ridge has been studied in various contexts. In statistical signal processing, ridges of functions or data clouds have been studied under the concept of principal curves (Hastie and Stuetzle, 1989; Kégl et al., 2002; Ozertem and Erdogmus, 2011). In images conditions for pixels being on the ridges are also discussed (Eberly, 1996; Miller, 1998). Although these previous works defined local conditions for ridges or samples from the principal curves, they do not answer the connectivity of such samples in space (Eberly, 1996; Miller, 1998; Ozertem and Erdogmus, 2011).

Earlier attempts to uncover the connectivity of samples from ridges used the topological skeletonization of data. The skeleton of an object is obtained by removing the exterior pixels/voxels to obtain the underlying geometry (centerline) of the structure (Cohen et al., 1994; Lee et al., 1994; Palágyi and Kuba, 1998). These morphological methods applied to binary data where segmented images are already provided beforehand, are very sensitive to noise level, resulting in disconnections in the skeleton.

Another set of algorithms employ active contour models or level-sets. These techniques optimize some suitable energy function that combines appearance and geometry terms through scalarization (e.g. linear combination). Unlike unsupervised clustering based approaches, prior shape models can also be incorporated into the optimization, which can be solved by efficient graph path search algorithms, such as Dijkstra's (Deschamps and Cohen, 2001; Schmitt et al., 2004; Vasilkoski and Stepanyants, 2009; Cherkassky et al., 1996). Shape priors are incorporated to the optimized energy function (Osher and Sethian, 1988; Mikaël et al., 2003; Nain et al., 2004; Schmitt et al., 2004; Cai et al., 2006; Wang et al., 2007; Zhou et al., 2008) to highlight the object boundaries. These approaches are shown to work well in a variety of scenarios for segmentation with careful tuning. However, tuning operation requires a detailed level of topological and structural understanding of the dataset in order to define energy functions that will succeed.

In conjunction with the contour models, multi-scale enhancement methods have also been employed to highlight certain curvilinear structures (Sato et al., 1998; Frangi et al., 1999; Deschamps and Cohen, 2001; Streekstra and van Pelt, 2002; Meijering et al., 2004; Wink et al., 2004; Zhu et al., 2009; Santamaría-Pang et al., 2007; González et al., 2010). Eigenanalysis of the Hessian matrix

of the image intensity is a popular approach to identify objects (e.g. vessels), where eigenvalue ratios can be related to local curvature.

In general, a major challenge in graph construction is parameter optimization. It is possible to end up with global solutions that are infeasible due to the selection of parameters or initializations, and tuning of these parameters get harder as the dimension of data increases. For that reason, most of the proposed 3D methods seek 3D associations between 2D image segmentation results (Wang et al., 2007; Schmitt et al., 2004; Cai et al., 2006, 2008; Zhang et al., 2008). However, such approaches increase the complexity by creating problems not present in 3D (e.g., occlusions), and try to address them with arbitrary heuristics.

In another track of algorithms, local 3D approaches construct a local graph representation for the data to simplify the search space without introducing complexity. For large datasets, where search space increases exponentially with the data dimension, these methods provide fast and efficient locally optimum solutions for the tracing problem (Al-Kofahi et al., 2002; Cai et al., 2006; Wang et al., 2007; Cai et al., 2008; Zhang et al., 2008). Algorithms in this category generally start from a given seed point with an initial direction vector. Optimality measures are similar to the ones that are defined for the global solutions, but they process only the proximity of the points in the feature space. Therefore they are also called "exploratory algorithms" which provide fast solutions for the optimum trace/minumum path problem. Generalized shape models can be classified in this category, where tubular objects are modeled as piecewise-linear cylinders with varying radius (Kitamura et al., 1988; Frangi et al., 1999; Al-Kofahi et al., 2002, 2003; Cruz et al., 2004; Bas and Erdogmus, 2010a). These methods locally fit the shape model to the wall of the tubular objects. Usually the shape is assumed to be a cylinder, but it can be more complex (superellipsoid) depending on the available computational power (Tyrrell et al., 2007) or simpler (sphere) depending on the application (Lesage et al., 2008).

Brainbow images, as shown in Fig. 1, are obtained by a recently developed technique for acquiring 3D colored confocal microscopy imagery that depict neuronal networks in the central nervous system (Livet et al., 2007; Hampel et al., 2011). They present a great opportunity for neuroscientists to study brain structure and function. By staining individual neurons using a combination of fluorescent proteins, each neuron can potentially be labeled with a distinct color (a maximum of approximately 90). However, given the complexity and the density of arboring structures, as well as due to the randomness in the staining process and protein expression, selectivity on the color labeling is limited, which results in similar labeling of distinct fibers in a vicinity. This is an active research area and more robust imaging techniques have been proposed to tackle such challenges (Lichtman et al., 2008).

Currently, researchers using Brainbow technology are limited to manual segmentation of images and tracing of axons to identify neural networks; this process is clearly cumbersome and prevents the study of large brain sections. The speed of progress is hampered by the inability to automatically extract structural information about the network from these images due to the lack of robust

and reliable 3D tubular object segmentation techniques for color images that could automatically trace axons.

Morphology information is also crucial for reliable stereological analysis and/or electrophysiological simulations (Ascoli et al., 2007). The quality of centerline estimation is the driving factor for accurate morphology extraction, and can be estimated with or without initial shape information. Based on (Bas and Erdogmus, 2010a,b), we describe two exploratory algorithms that can be used for tracing tubular structures in 3D color imagery, where the first one uses piecewise linear cylinder model to segment a fiber with varying radius, and the second one is a principal curve tracing algorithm that traces the centerline of the curvilinear structure through space.

We tested the algorithms on Brainbow images displaying a bundle of axons of motor neurons as shown in Fig. 1. In the sample we used, aferomentioned color diversity was limited and noise made the colors impure leading to spectral variations along axonal trace proles and their cross-sections (Lu, 2011). Compared to other datasets, these motor neuron images are harder to segment and trace since (*i*) they are very close or touching each other, (*ii*) the whole neuron fiber group is elongated in a stack. Consequently, 2D based gray level tracing methods, i.e. Maximum Intensity Projection (MIP) tracing, can not be directly applied to this dataset due to occlusions, close fiber interactions, and variations throughout the image. Most 3D methods rely on appearance and orientation with well separated fiber structures forming sparse clusters in space, which also make them inapplicable to this dataset.

A common challenge in tracing is the presence of gaps. Decisions based on a restricted local neighborhood that could not capture the nearby variations might result in suboptimal traces. The particular dataset used in the experiments does not have any fiber bifurcations. As a result of this, tracing of bifurcated fiber bundles are left out from the current discussion. Literature is vast on how to analyze such tree structured objects. Different approaches can be considered to tackle this problem: (*i*) manual branch point selection, (*ii*) exhaustively processing the whole data for critical point detection, and *(iii)* online decision mechanisms. However, only very few methods exist for exploratory algorithms in the literature and they are mostly nested decision algorithms, which are not always reliable and are not based on the inherited biological process.

The main contributions of the paper are as follows: first, to the extent of our knowledge, there is no segmentation or tracing algorithm for volumetric color images implemented before. However, some existing methods are easy to modify for this purpose. Second, we introduce adaptive subspace constrained local maxima analysis for the tracing of tubular structures in biomedical images, where initial segmentation is not available or cannot be obtained with naive thresholding methods.

2. Methods

Curvilinear structures, such as neuronal arbors, lie on locally 1D manifolds with spatial continuity in 3D space. Methods described here mainly aim to

extract the centerline of such structures. We started with a shape driven approach that assumes neuron fibers have tubular structure and model the curvilinear structure with a cylinder compartment model. Similar to the flux based approaches utilizing both regional and boundary terms, our method uses the gradient field of color images to define the boundary of objects and unlike conventional approaches in the literature, uses regional color information and alignment to trace the objects in dense regions. A local compartment model is adaptively tted to data based on an appearance and shape model to segment and trace the object in consecutive steps. However, most neurons (including the fiber set that we study here) have non-tubular and irregular shapes around their centerline/trace and our observations on the performance of the proposed flux based approach (Section 2.1) on noisy data led us to develop and implement our second approach, namely Principal Curve Tracing (PCT) (Section 2.2). This novel tracing approach is based on the concept of local subspace maxima denitions that have been introduced by Eberly et al. (Eberly, 1996) for image processing and later studied by (Ozertem and Erdogmus, 2011) et al. in statistical learning. In this approach, starting at an arbitrary location, we projected a sample to its underlying manifold, i.e. the principal curve, and span the underlying manifold with subspace constrained tracing iterations. In the following sections, we assume that the initial seed location $\mathbf{x}_0$ and tracing direction ($\mathbf{n}_0$) are given.

2.1. Piecewise Linear Cylindrical Model (PLCM)

In order to build a compartment model, we assume that axons are tubular shaped structures having circular cross sections orthogonal to their axis directions. Our PLCM approach involves building piecewise linear cylinder approximations starting from a single seed point inside an axon given by the user. For a given seed voxel, the algorithm highlights each axon through a two-step process. The first step (tuning) calculates the local axis orientation and the corresponding perpendicular circular cross-section of the axon, and the second step (propagation) identifies a cylinder compartment with the given circular base and orientation that approximates the curved axon in a piecewise linear fashion. The process is iteratively repeated to identify a piecewise linear cylinder model of the axon starting from the initial seed.

2.1.1. Preprocessing of 3D image stack

In order to find piecewise linear cylinder compartments with varying orientation, length and radius, we first estimate the fiber boundary by calculating the edge strength over the feature space. Since the point spread function of the imaging modality is not isotropic in space, each image slice is resampled to achieve cubical voxels. Then a preprocessing step is utilized, where the image volume is smoothed using 3D bilateral filtering (Tomasi and Manduchi, 1998). Fig. 1(b-c) depict the raw and denoised image patches highlighted with the red square in Fig. 1(a). We used a similar strategy to the one described for 2D color images in (Lee and Cok, 1991) to calculate the edge strength. Specifically we

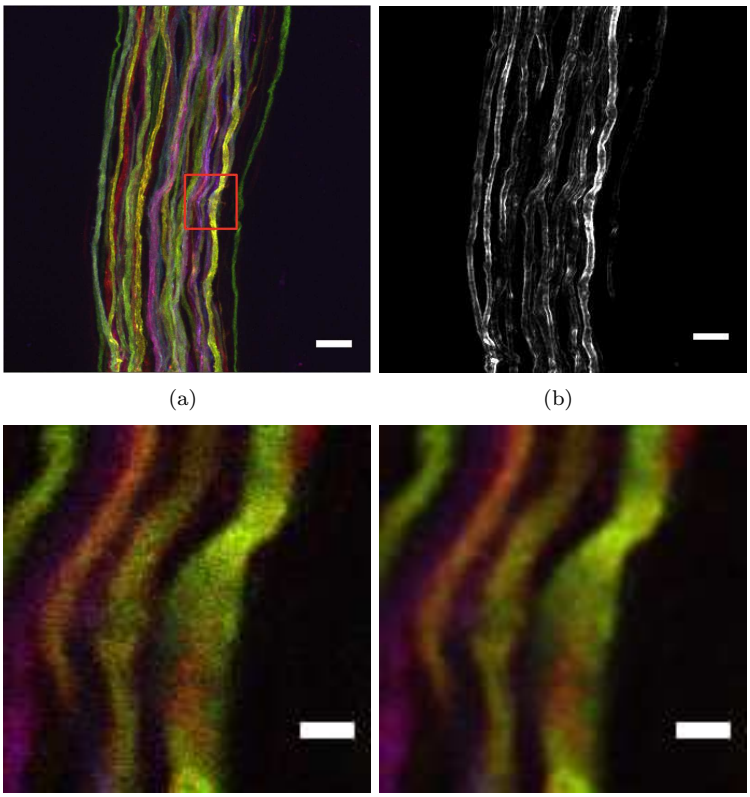

Figure 1: (a) MIP of brainbow image stack showing a bundle of axons of motor neurons. (b) MIP of estimated edge map of the image stack. (c) Zoomed single slice view of the region depicted with red box in (a). (d) Same region after 3D bilateral denoising. Scale bars are 100 pixels in (a-b) and 20 pixels in (c-d) respectively.

used the largest singular value of the color Jacobian with respect to voxel coordinates. The largest singular value of a color Jacobian matrix reduces to the gradient norm for single channel (gray level) images, and has been proven to be more robust to noise as discussed in the same work. The (RGB) color Jacobian with respect to position (xyz, where z is depth across image slices obtained via confocal microscopy) is

$$\mathbf{J} = \frac{\partial \mathbf{c}}{\partial \mathbf{x}} = \begin{bmatrix} \frac{dR}{dx} & \frac{dR}{dy} & \frac{dR}{dz} \\ \frac{dG}{dx} & \frac{dG}{dy} & \frac{dG}{dz} \\ \frac{dB}{dx} & \frac{dB}{dy} & \frac{dB}{dz} \end{bmatrix} \tag{1}$$

Here $\mathbf{c} \in \mathbb{R}^3$ and $\mathbf{x} \in \mathbb{R}^3$ are color-feature vector and position-vector respectively. The edge map is calculated by assigning an edgeness value to each voxel, where edgeness is defined as the largest singular value of $\mathbf{J}$. A MIP of the obtained 3D

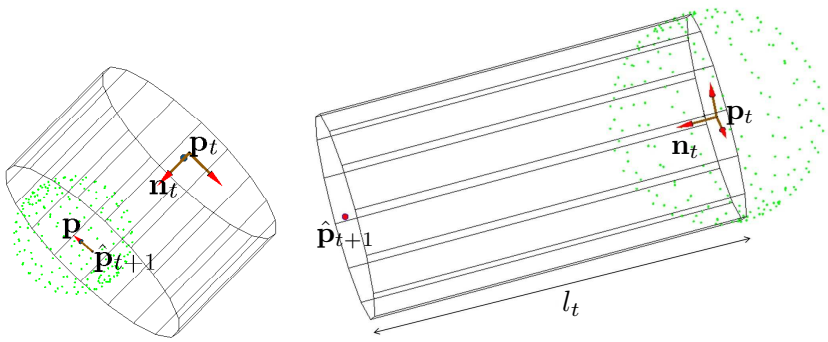

(a) Tuning Step (b) Propagation Step

Figure 2: Tuning and propagation steps are illustrated: (a) Tuning consists of finding a sphere with center p_0 and radius r_0, as well as finding the axon propagation direction $\mathbf{n}$, which specifies a circular base for the local cylinder. (b) Propagation identifies the length l of the piecewise cylinder such that the surface of the cylinder follows the strong edges and the interior has a consistent color.

edge map is depicted in Fig. 1(b). The calculated edge map is used to define the edgeness of any point in space via 3D-cubic spline interpolation. We denote the edgeness of any arbitrary point $\mathbf{s}$ as $\mathbf{E}(\mathbf{s})$.

2.1.2. Tuning

Let $\mathbf{C}_t$ be the tth cylinder compartment with the initial circular surface centered at $\mathbf{x}_t$ having radius r_t and axial vector $\mathbf{n}_t$ as illustrated in Fig. 2). For a given initial seed $\mathbf{x}_0$ or a center estimated after the propagation step from the tth compartment $\mathbf{C}_t$ given by $\hat{\mathbf{x}}_{t+1} = \mathbf{x}_t + l_t\mathbf{n}_t$, we optimally identify the center $\mathbf{x}_{t+1}$, radius r_{t+1}, and direction $\mathbf{n}_{t+1}$ of the axon via the following procedure:

Step 1: In order to identify the center $\mathbf{x}_{t+1}$ and radius r_{t+1} of the compartment $\mathbf{C}_{t+1}$, we used a sphere model to fit the local curvilinear structure by formulating a constrained optimization. We optimally find the center $\mathbf{x}_{t+1}$ and radius r_{t+1} by maximizing the overall edgeness on the sphere surface by constraining the solution set to result in continuous compartments in spatial and color space. Objective function of the formulation (2) is based on the overall edgeness on the surface and defined as the total edgeness values $(\mathbf{E}(\mathbf{s}_t; \mathbf{x}, r))$ on sample points $\mathbf{s}_t$ from the surface of sphere $S(\mathbf{x}; r)$. Here, $\mathbf{s}_t$ are obtained using uniformly displaced grid samples on the sphere (Bauer, 2000) and the edgeness of a sample is obtained from the edge map via 3D-cubic spline interpolation as mentioned before. Solution of the optimization problem is achieved

by employing an active-set algorithm (Fletcher and Powell, 1963).

$$
\begin{aligned}
(\mathbf{x}_{t+1}, r_{t+1}) &= \arg\max_{\mathbf{x},r} \sum_i \mathbf{E}(\mathbf{s}_t; \mathbf{x}, r) \text{ subject to} && (2)\\
& \quad \mathbf{n}_t^T(\mathbf{x} - \hat{\mathbf{x}}_{t+1}) = 0 && (i)\\
& \quad (\mathbf{I} - \mathbf{n}_t\mathbf{n}_t^T)(\mathbf{x} - \hat{\mathbf{x}}_{t+1}) < r_t && (ii)\\
& \quad \cos(\text{angle}) > 0.9 && (iii)
\end{aligned}
$$

where $\mathbf{I} \in \mathbb{R}^{3x3}$ is the identity matrix.

Continuity of the compartments is guaranteed by constraining the optimization such that (i) the center of the the new sphere lies on the plane that is defined by the last circular surface of the previous cylinder, (ii) the center of the new sphere must be within r_t distance from $\hat{\mathbf{x}}_t$, (iii) the cos(angle) between the color distributions of voxels in previous cylinder and current sphere must be greater than 0.9. Constraints (i) and (ii) assure that compartments have continuity in spatial space and mainly affect the optimization of $\mathbf{x}$, whereas (iii) is more related with continuity in color space and act as a limiting factor for $\mathbf{r}$. Instead of directly constraining the color values of voxels, we utilize a more probabilistic approach for the color continuity that also takes into local color variations by calculating the cosine of the angle between the color distributions of the fiber compartment $\mathbf{C}_t$ and the sphere $S(\mathbf{x}; r)$. We used an interior point algorithm (Waltz et al., 2006) to solve the above optimization problem.

Let $\mathbf{m}_t$ & $\mathbf{\Sigma}_t$ and $\mathbf{m}_{S(\mathbf{x},r)}$ & $\mathbf{\Sigma}_{S(\mathbf{x},r)}$ be the estimated mean and covariances of the Gaussian color distribution model in decorrelated RGB color space for the voxels in the last cylinder compartment $\mathbf{C}_t$ and the current sphere $S(\mathbf{x}; r)$. The color distributions are assumed to be Gaussian
$G(\mathbf{x}, \mathbf{\Sigma}) = (2\pi)^{-3/2} \det(\mathbf{\Sigma})^{-1/2} \exp(-\frac{1}{2}\mathbf{x}^T\mathbf{\Sigma}^{-1}\mathbf{x})$ and the mean and covariance estimates are obtained using Expectation-Maximization (EM) (Dempster et al., 1977).

The inner product between two Gaussian densities $G_j = G(\mathbf{x} - \mathbf{m}_j; \mathbf{\Sigma}_j)$ for $j = 1, 2$ can be written as $< G_1, G_2 >= \int G(\mathbf{x} - \mathbf{m}_1; \mathbf{\Sigma}_1)G(\mathbf{x} - \mathbf{m}_2; \mathbf{\Sigma}_2)d\mathbf{x}$, then the third constrain (iii) can be formulated as

$$
\begin{aligned}
\cos(\text{angle}) &= \frac{< G_1, G_2 >}{(< G_1, G_1 >< G_2, G_2 >)^{1/2}} && (3)\\
&= \frac{G(\mathbf{m}_1 - \mathbf{m}_2; \mathbf{\Sigma}_1 + \mathbf{\Sigma}_2)}{G(\mathbf{0}; 2\mathbf{\Sigma}_1)G(\mathbf{0}; 2\mathbf{\Sigma}_2)}
\end{aligned}
$$

In Brainbow imagery, distinct colors (a maximum of approximately 90) are used to label different fibers. However, in the sample we used, this color diversity was more limited and noise made the colors impure leading to spectral variations in the cross-section and along the trace profiles of fibers. Decorrelation techniques (Alley, 1996) can be applied to enhance color diversity between axons, but these methods may also change the image intensity and its gradient, and introduce arbitrary edges to the imageset. For that reason, decorrelated

Algorithm 1 Tracing of Curvilinear structures in 3D Images using PLCM

Given $\mathbf{E}$, thr_{L}, thr_{U} at iteration t=0 initialize $\mathbf{x}_0$, and the initial direction of the curve $\mathbf{n}_0$.
while $\mathbf{x}$ is inside the image boundary **do**
  procedure ITERATEVOXEL($\mathbf{x}_t$, $\mathbf{n}_t$, $\mathbf{E}$)
    Maximize (2) to find the location $\mathbf{x}_{t+1}$ and the radius r_{t+1} ▷ Step1
    Find the propagation direction,$\mathbf{n}_{t+1}$, based on the eigendecomposition of (5) ▷ Step2
    Estimate the optimum length, L_{t+1}, using (6).
    Update $\mathbf{x}_{t+1} \leftarrow \mathbf{x}_{t+1} + L_{t+1}\mathbf{n}_{t+1}$ ▷ Propagation
    return $\mathbf{x}_{t+1}$, $\mathbf{n}_{t+1}$
  end procedure
end while

color space is used to constrain the optimization problem defined in (2) without changing the original edges calculated in RGB color space. In order to decorrelate the image we applied the following whitening transformation

$$\overline{\mathbf{U}} = \mathbf{V}\mathbf{D}^{-1/2}\mathbf{V}^T\mathbf{U} \tag{4}$$

Here $\mathbf{V}$ is the basis matrix whose columns are the eigenvectors of the covariance of the data matrix $\mathbf{U} \in \mathbb{R}^{3xN}$, where N is the number of voxels in the dataset and each column corresponds to a voxel color value. $\mathbf{D}^{-1/2}$ is the diagonal stretching matrix having values $\varsigma[\kappa_1^{-1/2}, \kappa_2^{-1/2}, \kappa_3^{-1/2}]$, where ς is the desired standard deviation in each color channel and κ_t's are the eigenvalues of the covariance of the color data. This way each transformed color channel will have the same range of brightness and variance. This particular choice of enhancement method is arbitrary, and can be potentially replaced with other methods to improve color diversity.

Step 2: The direction $\mathbf{n}_{t+1}$ is identified as the eigenvector corresponding to the largest eigenvalue of a weighted covariance matrix $\mathbf{W}$ of voxel coordinate vectors for each voxel $\mathbf{v}_j$ in a bounding cube that contains sphere $S(\mathbf{x}_{t+1}, r_{t+1})$. The weight of each voxel is obtained from the Gaussian color model identified from the voxels inside the sphere using EM as described in step (1). Specifically:

$$\mathbf{W} = \sum_j G(\mathbf{d}_j; s^2\mathbf{I}) G(\mathbf{c}_j - \mathbf{m}_{S_{t+1}}; \mathbf{\Sigma}_{S_{t+1}}) \|\mathbf{n}_t^T \mathbf{d}_j\| \mathbf{d}_j \mathbf{d}_j^T \tag{5}$$

where $\mathbf{c}_j$ is the color of voxel $\mathbf{v}_j$ and $\mathbf{d}_j = \mathbf{v}_j - \mathbf{x}_{t+1}$ is the displacement of voxel $\mathbf{v}_j$ from the center of the current sphere $S_{t+1} = S(\mathbf{x}_{t+1}, r_{t+1})$, and s^2 is the scale parameter of the spatial model. Sign of the eigenvector is selected such that it makes a positive inner product with $\mathbf{n}_t$, such that $\mathbf{W} = \sum_{i=1}^{3} \gamma_i \mathbf{w}_i \mathbf{w}_i^T$ and $\mathbf{n}_{t+1} = \mathrm{sign}(\mathbf{n}_t^T \mathbf{w}_1)\mathbf{w}_1$ where $\mathbf{w}_i$ and γ_i are the eigenvector/value pair of $\mathbf{W}$ and $\gamma_1 > \cdots > \gamma_3$. The outline of the PLCM algorithm is given in Alg. 1.

2.1.3. Propagation

In order to calculate the base and the length (L) of the cylinder compartment, we first projected the sphere $S(\mathbf{x}_{t+1}, r_{t+1})$ obtained in the previous tuning step onto the plane defined by the direction vector $\mathbf{n}_{t+1}$, and denoted this circle as $B(\mathbf{x}_{t+1}, r_{t+1}, \mathbf{n}_{t+1})$. The obtained base (a circle having normal vector $\mathbf{n}_{t+1}$) is assumed as the reference for the cylinder compartment and a line search is employed to find the length of the whole compartment. The length of the compartment is selected adaptively with respect to the reference cylinder (initial circle) by constraining the edgeness on the lateral surface of the compartment. The length of the tth compartment is given as

$$\begin{aligned} L_{t+1} &= \arg\max_{l} \sum_{k} \mathbf{E}(\mathbf{q}_k; C(\mathbf{x}_{t+1}, r_{t+1}, l\mathbf{n}_{t+1})) \text{ subject to} \\ & \quad thr_{\mathrm{L}} < \frac{\sum_k \mathbf{E}(\mathbf{q}_k; C(\mathbf{x}_{t+1}, r_{t+1}, l\mathbf{n}_{t+1}))}{l \sum_j \mathbf{E}(\mathbf{s}_j; B(\mathbf{x}_{t+1}, r_{t+1}, \mathbf{n}_{+1}))} < thr_{\mathrm{U}} \end{aligned} \tag{6}$$

where $C(\mathbf{x}_{t+1}, r_{t+1}, l\mathbf{n}_{t+1})$ is a cylinder with base center $\mathbf{x}_{t+1}$, radius r_{t+1}, with length l in the direction of $\mathbf{n}_{t+1}$, and $\mathbf{q}_k$ are samples from its surface taken on a uniform grid along the angle of the circular base (with $\pi/10$ rad resolution) and length (at a resolution of one voxel). Similarly, $B(\mathbf{x}_{t+1}, r_{t+1}, \mathbf{n}_t)$ is the base of this cylinder and $\mathbf{s}_j$ are samples taken uniformly from its circular boundary (at $\pi/10$ rad sample period). The defined criterion seeks a cylinder compartment that maximizes the overall edgeness on the lateral surface similar to the one defined in (2). However, unless some additional constraints are introduced to the formulation, the optimization procedure ends up with a trivial solution ($L = \infty$). In order to adapt to the local variations of the neuronal arbors, we constrained the overall edgeness by lower and upper bounds with respect to the reference base $B(\mathbf{x}_{t+1}, r_{t+1}, \mathbf{n}_t)$. Specifically, we have used $thr_{\mathrm{L}} = 0.98$ and $thr_{\mathrm{U}} = 1.05$ as lower and upper thresholds, respectively.

2.2. Principal Curve Tracing

In the previous section, we described a vectorial tracing procedure that segments fiber tracks by jointly optimizing the radius, r_t and center location, $\mathbf{x}_t$. Neuronal arbors, in general, form fiber bundles and have arbitrary shapes in their axonal crossection, which limits the effectiveness of flux or tubeness based approaches. Moreover, a common problem with such approaches, e.g. Frangi filter, is the inability to distinguish neighbor fibers, if the distance between fibers is small compared to the radius of fibers, like the fibers in this study. Consequently, artifacts that are due to lack of resolution, such as crossovers, results in merging of fibers/vessels or even creates artificial ridges between fibers. Moreover, centerline extraction procedure can be separated from the volume segmentation and the diameter of the branch can be estimated given its centerline/ridge (Meijering, 2010). However, such simplification in the extraction of the morphology increases the importance of the ridge estimation procedure.

In this section, we describe a mathematically rigorous ridge estimation technique based on the differential geometric properties of an object and utilizing local statistics obtained from data samples. A ridge/principal curve is a curve that passes through the "center" of a high dimensional data cloud or a multivariate scalar valued function. A rigorous way of defining the ridge of a function is to check the local critical set/manifold definitions (Eberly, 1996; Ozertem and Erdogmus, 2011). Let $f(\mathbf{x}) : \mathbb{R}^n \to \mathbb{R}$ be an at least twice continuously differentiable function, $\mathbf{g}(\mathbf{x})$ and $\mathbf{H}(\mathbf{x})$ be its gradient and Hessian. Let $\mathbf{q}_i$ and λ_i be the ith eigenvector/value pair of the Hessian matrix of $f(\mathbf{x})$ such that $\lambda_1 \leq \cdots \leq \lambda_n$. In general, a point is on the d-dimensional principal manifold iff the gradient is orthogonal to $n-d$ eigenvectors, $\mathbf{g}(\mathbf{x})^T\mathbf{q}_i(\mathbf{x}) = 0$, and the eigenvalues corresponding to these eigenvectors are all negative, $\lambda_{d+1}, \ldots, \lambda_i, \ldots, \lambda_n < 0$. Since our goal is to extract 1D centerline information, we will assume $d = 1$ in the rest of the paper.

These local conditions are generalizations of the local maxima/minima conditions; a point on the ridge is the local maximum of the function in the subspace spanned by the $n-1$ eigenvectors, $S_\perp = \text{span}(\mathbf{q}_2, \ldots, \mathbf{q}_n)$. Similarly, tangential space is spanned by the remaining 1 eigenvector, $S_\parallel = \text{span}(\mathbf{q}_1)$. Let $\mathbf{H}_\perp(\mathbf{x}) = \sum_2^n(\lambda_i\mathbf{q}_i\mathbf{q}_i^T)$ and $\mathbf{H}_\parallel(\mathbf{x}) = \mathbf{H}(\mathbf{x}) - \mathbf{H}_\perp(\mathbf{x})$ be the orthogonal and parallel component of $\mathbf{H}(\mathbf{x})$; a measure for being on the ridge can be formulated as

$$\zeta(\mathbf{x}) = \text{abs}(\frac{\mathbf{g}(\mathbf{x})^T\mathbf{H}_\perp(\mathbf{x})\mathbf{g}(\mathbf{x})}{\|\mathbf{H}(\mathbf{x})\mathbf{g}(\mathbf{x})\|\|\mathbf{g}(\mathbf{x})\|}) \tag{7}$$

Using local conditions and the measure for being on the ridge, we developed a principal curve tracing algorithm to extract the connectivity of neuronal arbors. Similar to the shape model based tracing technique that we outlined in Sec. 2.1, the developed technique uses color and spatial information to trace the fiber. However, instead of incorporating the color and position directly, PCT algorithm builds an spatial-appearance model that discriminates nearby fibers without explicitly using the edge information. Moreover, the algorithm uses the gradient and Hessian of the ridge function to calculate the principal curves as the underlying structures to trace the neuronal arbors separately. Similar to the PLCM method, PCT algorithm has two important steps: i)projection/tuning and ii) tracing/propagation. In order to not mix the definitions, we use projection and tracing terms to explain the concept of PCT here.

As a matter of fact, given a ridge function, by solving an ordinary differential equation (ODE) using numerical integration methods, e.g. Euler (Ascher and Petzold, 1998), iterations constrained to the normal space project any arbitrary sample point to its underlying principal curve. Termination of the projection is decided based on the measure given in (7), i.e. $\zeta(\mathbf{x}) = 0$. Likewise, fixed step size or fixed-length updates can be used to trace the curve along the center of the data. As a result, updates constrained to $S_\perp(\mathbf{x})$ will converge to the principal curves given the proper update direction, whereas propagating through tangential vector $S_\parallel(\mathbf{x})$ will trace the locally defined principal curve at $\mathbf{x}$. So, similar to PLCM, an iterative tracing algorithm using a correction-update scheme is

possible by incorporating the iterations on the normal plane (projection/tuning step) and the tangential vector (tracing/propagation step) with proper directions. Selection of the direction for the projection is straightforward. In order for projected samples to converge to the nearby principal curve, a direction that increases the function value, ($f(\mathbf{x})$), is selected such that the projection updates make positive inner product with the gradient, ($\mathbf{g}(\mathbf{x})$), at each iteration. In addition, given an initial tracing direction, direction of tracing is selected so that it makes positive inner product with the tracing update of the previous iteration. The outline of the PCT algorithm is given in Alg. 2.

Algorithm 2 Summary of Principal Curve Tracing Algorithm

```
At iteration t=0 initialize x_0, the step sizes μ_⊥, μ_∥, thr, and the direction of
the curve n_0. (d=1)
while f(x) > thr do
    IterateSample(x,X,μ_⊥, μ_∥,n_t)
    t ← t + 1
end while
procedure IterateSample(x, X,μ_⊥, μ_∥,n_0)
    ζ(x) = ∞
    while ζ(x) > 0 do                                  ▷ Correction/Projection Step
        Evaluate f(x), g(x), H(x), and ζ(x)
        if f(x) < thr then
            stop
        end if
        Perform the eigendecomposition of H(x) = VΓV,
        where V_{1:n} are the eigenvectors with corresponding
        eigenvalues Γ = diag{λ_1 ≤ λ_2 ≤ ··· ≤ λ_n}.
        x ← x + μ_⊥ V_{2:n} V_{2:n}^T g(x)
        return x
    end while
    n_t = V_1 sign(V_1^T n_{t−1})                      ▷ Tracing/Propagation Step
    x ← x + μ_∥ n_t
    return x, n_t
end procedure
```

2.2.1. Estimation of The Ridge Function -$f(\mathbf{x})$

In order to construct an at least twice continuously differentiable function, we used the weighted Gaussian kernel density estimation method (Silverman, 1998). KDE is used as an example since it encompasses parametric mixture models as a special case; however the outlined method is general for any pdf model. Consider a general weighted variable-width kernel density estimate obtained from samples $\mathbf{X} = \mathbf{x}_1, \ldots, \mathbf{x}_N$. Weighted KDE is given as

$$p(\mathbf{x}) = \sum_{i=1}^{N} w(\mathbf{x}_i) G_{\mathbf{\Sigma}_i}(\mathbf{x} - \mathbf{x}_i) \tag{8}$$

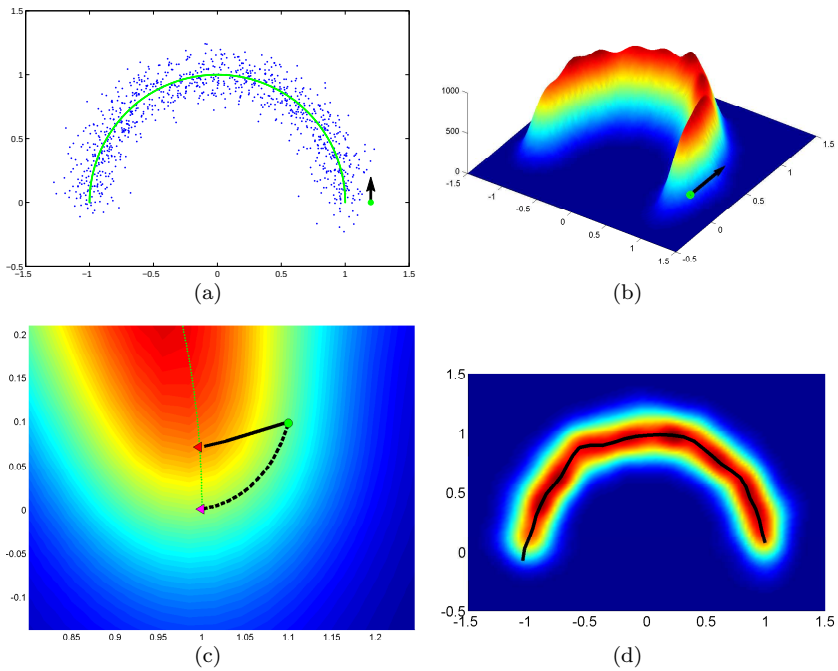

Figure 3: Tracing of semicircular data. (a) Data is generated using a semi-circle curve with radially perturbed noise (n=2 and d=1). Initial seed and tracing direction is depicted with green dot and black arrow. (b) Estimated probability density ($p(\mathbf{x})$). (c) Two different projection trajectory. Solid line is obtained using the Hessian of the $f(\mathbf{x}) = \log(p(\mathbf{x}))$, where as the Hessian of the ($p(\mathbf{x})$) results in a curvy trajectory. (d) Result of the PCT algorithm.

where $w(\mathbf{x}_i)$ is the weight and $\mathbf{\Sigma}_i$ is the variable kernel covariance of the kernel.

Selection of kernel type is arbitrary, and here we utilized the Gaussian kernel for its simplicity and popularity. For the ith data sample $\mathbf{x}_i$, the Gaussian kernel is given as $G_{\mathbf{\Sigma}_i}(\mathbf{x} - \mathbf{x_i}) = C_{\mathbf{\Sigma}_i} e^{-\frac{1}{2}(\mathbf{x}-\mathbf{x}_i)^T \mathbf{\Sigma}_i^{-1}(\mathbf{x}-\mathbf{x}_i)}$. The gradient and the Hessian of the KDE are:

$$\mathbf{g}(\mathbf{x}) = -\sum_{i=1}^{N} w(\mathbf{x}_i) G_{\mathbf{\Sigma}_i}(\mathbf{x} - \mathbf{x}_i)\mathbf{u}_i \tag{9}$$

$$\mathbf{C}(\mathbf{x}) = \sum_{i=1}^{N} w(\mathbf{x}_i) G_{\mathbf{\Sigma}_i}(\mathbf{x} - \mathbf{x}_i)(\mathbf{u}_i \mathbf{u}_i^T - \mathbf{\Sigma}_i^{-1}) \tag{10}$$

Here $\mathbf{u}_i = \mathbf{\Sigma}_i^{-1}(\mathbf{x} - \mathbf{x}_i)$.

Since any monotonically increasing function does not change the critical set

of the given function[1], we defined $f(\mathbf{x}) = \log(p(\mathbf{x}))$ in order for principal curve projections to be consistent with PCA projections in the case of a Gaussian density. Instead of using the Hessian of $p(\mathbf{x})$, we estimated the normal space from the Hessian of $f(\mathbf{x})$ given as:

$$\begin{aligned} \mathbf{H}(\mathbf{x}) &= \frac{\partial^2 f}{\partial \mathbf{x} \partial \mathbf{x}^T} = \mathbf{C}_{\log(p(\mathbf{x}))}(\mathbf{x}) \\ &= -p^{-1}(\mathbf{x})\mathbf{C}(\mathbf{x}) + p^{-2}(\mathbf{x})\mathbf{g}(\mathbf{x})^T\mathbf{g}(\mathbf{x}) \end{aligned} \tag{11}$$

By taking the logarithm of the density function $p(\mathbf{x})$, we introduced additional computational load to the algorithm. However, by applying such a transform, our goal is to linearize the trajectory of PCT projections in the correction step, resulting in more straight projection trajectories. Fig. 3(a) shows a synthetic semicircular data perturbed by radial Gaussian noise ($\mathcal{N}(0,1)$). Underlying ridge function is denoted with the green semicircle. The black arrow represents the initial tracing direction and the green circle shows the initial starting point. Fig. 3(b) displays the obtained kernel density function, ($p(\mathbf{x})$). Fig. 3(c) shows the effect of using a monotonic function to linearize the projection trajectory. Projection with respect to the Hessian of $p(\mathbf{x})$, $\mathbf{C}$, is depicted with a black dashed line, whereas the trajectory employing the Hessian of $f(\mathbf{x}) = \log(p(\mathbf{x}))$, $\mathbf{H}$, is displayed with a black solid line. The initial seed is the same for both projections and is selected as $\mathbf{x}_0 = [1.1; 0.1]$. Although they converge to the same principal curve, the trajectories of subspace projections employing $\mathbf{C}$ and $\mathbf{H}$, consequently the corresponding coordinates on the principal curve, vary. Colored triangles (red and magenta) represent the projected initial seed based on $\mathbf{H}$ and $\mathbf{C}$, respectively. Note that both iterations converge to the same underlying principal curve successfully. Nevertheless, number of iterations needed until convergence is 271 for $\mathbf{C}$, whereas 53 for $\mathbf{H}$ in this particular example ($\mu_\perp = 0.01$). Once the initial seed is projected onto the principal curve, the underling curve is traced using the correction and the tracing steps iteratively as outlined in Alg.2. After each tracing update ($\mathbf{x} \leftarrow \mathbf{x} + \mu_\parallel \mathbf{n}_t$), the correction step pulls the diverged iteration towards the underlying principal curve. Fig. 3(d) displays the result of the PCT algorithm in black color. Here and in the remainder of the paper, we used $\mathbf{H}$ to estimate the normal subspace.

2.2.2. Principal Curves for Fiber Tracing in Volumetric Images

In volumetric images, color values ($\mathbf{c} \in \mathbb{R}^3$) and pixel locations ($\mathbf{p} \in \mathbb{R}^3$) form the feature space, however color values lie on the manifold described by the spatial space. Additionally, it is known that kernel density estimate does not work well as the dimension increases due to the curse of dimensionality. Therefore, as a consequence of these two facts, rather than tracing the ridge of the weighted density described by feature $\mathbf{x} = [\mathbf{p}; \mathbf{c}]$ jointly, we formulated the weighted KDE estimate based on the spatial variable ($\mathbf{x} \leftarrow \mathbf{p}$) only. This

[1]Since the first derivative of a monotonic function is always positive, derivative of the function after monotonic mapping has the same critical solutions due to the chain rule.

way, eigenanalysis is constrained only to the spatial domain, which reduces the dimensionality, increases the speed of the algorithm, and prevents possible errors due to high fluctuations in the color space, which will affect the selection of eigenvectors that forms the subspace for projections.

Moreover, in order to estimate the kernel density, isotropic fixed bandwidth kernels are employed for simplicity. Since gradient is collinear with the mean-shift updates for isotropic kernels, we replaced the fix-step iterations with adaptive mean-shift iterations (Comaniciu and Meer, 2002) in order to further speed-up the algorithm. Mean-shift (MS) updates are obtained by equating the gradient in (9) to zero and are in the form $\mathbf{x} \leftarrow \mathbf{ms}(\mathbf{x})$, where

$$\mathbf{ms}(\mathbf{x}) = (\sum_{i=1}^{N} G_{\mathbf{\Sigma}_i}(\mathbf{x}-\mathbf{x}_i)\mathbf{\Sigma}_i^{-1})^{-1} \sum_{i=1}^{N} G_{\mathbf{\Sigma}_i}(\mathbf{x}-\mathbf{x}_i)\mathbf{\Sigma}_i^{-1}\mathbf{x}_i \tag{12}$$

Note that MS updates are simply used to choose the projection direction and eliminates the need for selecting a step size $\mu_\perp$. Otherwise, it has no influence on the projection procedure, or the tracing steps.

In order to reduce computational load, KDE computations are restricted to the K-Nearest Neighbors (KNN) in space denoted by $N_{\mathbf{x}}^{KNN}$. Weights in KDE are selected as the pixel intensity values, $I(\mathbf{x})$ and the color similarity between voxels. Bounded-support Gaussian kernels are employed, $G_{\Sigma_i}(\mathbf{x}-\mathbf{x}_i) \leftarrow \alpha B_{2,\epsilon}(\mathbf{x}-\mathbf{x}_i)G_{\mathbf{\Sigma}_{i,p}}(\mathbf{x}-\mathbf{x}_i)$, constraining computations to neighboring pixels. Here, $\mathbf{x}_i$ is the position of a voxel in the neighborhood. $B_{2,\epsilon}(\mathbf{x}-\mathbf{x}_i)$ is the support ball with L_2 norm radius ϵ, and α is the normalization constant of the kernel. KDE becomes

$$\begin{aligned} p(\mathbf{x}) &= \sum_{i=1}^{N} I(\mathbf{x}_i)G_{\mathbf{\Sigma}_{i,c}}(\mathbf{c}-\mathbf{c}_i)\alpha B_{2,\epsilon}(\mathbf{x}-\mathbf{x}_i)G_{\mathbf{\Sigma}_{i,p}}(\mathbf{x}-\mathbf{x}_i) \\ &= \sum_{\mathbf{x}_i \in B_{2,\epsilon}(\mathbf{x})} w_i \alpha G_{\mathbf{\Sigma}_{i,p}}(\mathbf{x}-\mathbf{x}_i) \end{aligned} \tag{13}$$

where $w_i = I(\mathbf{x}_i)G_{\mathbf{\Sigma}_{i,c}}(\mathbf{c}-\mathbf{c}_i)$ is the weight of the ith kernel. Letting $\beta_i(\mathbf{x}) = \alpha w_i G_{\mathbf{\Sigma}_{i,p}}(\mathbf{x}-\mathbf{x}_i)$, the gradient and Hessian are

$$\mathbf{g}(\mathbf{x}) = -\sum_{\mathbf{x}_i \in B_{2,\epsilon}(\mathbf{x})} \beta_i(\mathbf{x})\Sigma_{i,p}^{-1}(\mathbf{x}-\mathbf{x}_i) \tag{14}$$

$$\mathbf{H}(\mathbf{x}) = \sum_{\mathbf{x}_i \in B_{2,\epsilon}(\mathbf{x})} \beta_i(\mathbf{x})(\Sigma_{i,p}^{-1}(\mathbf{x}-\mathbf{x}_i)(\mathbf{x}-\mathbf{x}_i)^T\mathbf{\Sigma}_{i,p}^{-1} - \mathbf{\Sigma}_{i,p}^{-1}) \tag{15}$$

Similarly, $\mathbf{ms}(\mathbf{x})$ is given as

$$\mathbf{ms}(\mathbf{x}) = (\sum_{\mathbf{x}_i \in B_{2,\epsilon}(\mathbf{x})} \beta_i(\mathbf{x})\Sigma_{i,p}^{-1})^{-1} \sum_{\mathbf{x}_i \in B_{2,\epsilon}(\mathbf{x})} \beta_i(\mathbf{x})\Sigma_{i,p}^{-1}\mathbf{x}_i \tag{16}$$

Algorithm 3 Tracing of Curvilinear structures in 3D Images using PCT

At iteration t=0 initialize $\mathbf{x}_0$, the step size $\mu_\parallel$, thr, and the initial direction of the curve $\mathbf{n}_0$. (n=3, d=1)
while $\mathbf{x}$ is inside the image boundary **do**
  procedure TRACEAXON($\mathbf{x}$, $B_{2,\epsilon}(\mathbf{x})$, $\mu_\parallel$,$\mathbf{n}_0$)
    IterateVoxel($\mathbf{x}$,$\mathbf{X}$, $\mu_\parallel$,$\mathbf{n}_t$)
    $t \leftarrow t+1$
  end procedure
end while
procedure ITERATEVOXEL($\mathbf{x}$, $B_{2,\epsilon}(\mathbf{x})$, $\mu_\parallel$,$\mathbf{n}_{t-1}$)
  $\zeta(\mathbf{x}) = \infty$
  while $\zeta(\mathbf{x}) > 0$ **do**
    Evaluate $f(\mathbf{x}), \mathbf{ms}(\mathbf{x})$, $\mathbf{H}(\mathbf{x})$, and $\zeta(\mathbf{x})$
    if $f(\mathbf{x}) < thr$ **then**
      stop
    end if
    Perform the eigendecomposition of $\mathbf{H}(\mathbf{x}) = \mathbf{V\Gamma V}$,
    where $\mathbf{V}_{1:n}$ are the eigenvectors with corresponding
    eigenvalues $\mathbf{\Gamma} = \mathbf{diag}\{\lambda_\mathbf{1} \leq \lambda_\mathbf{2} \leq \cdots \leq \lambda_\mathbf{n}\}$.
    $\mathbf{x} \leftarrow \mathbf{x} + \mathbf{V}_{2:n}\mathbf{V}_{2:n}^T\mathbf{ms}(\mathbf{x})$
    return $\mathbf{x}$
  end while
  $\mathbf{n}_t = \mathbf{V}_1 \text{sign}(\mathbf{V}_1^T\mathbf{n}_{t-1})$
  $\mathbf{x} \leftarrow \underset{\mathbf{x}_i \in T_\mathbf{x}}{\text{argmin}}(\mathbf{n}_t^T(\mathbf{x}_i - x)/\|(\mathbf{x}_i - x)\|)$ ▷ $T_\mathbf{x}$ is the connected neighborhood of the $\mathbf{x}$ composed of 26 voxels in 3D.
  return $\mathbf{x}$, $\mathbf{n}_t$
end procedure

Furthermore, in order to obtain continuous tracing over voxels, tracing iterations can be restricted to immediate spatially neighboring voxels as a part of vectorial tracing. Selection of the step size and kernel bandwidths are manual and proper selection should be determined by data geometry. Summary of the algorithm is presented in Alg. 3.

3. Results

We demonstrate the noise robustness of the proposed methods on synthetic data using 50 Monte-Carlo simulations. Data is composed of two curvilinear structures labeled with distinct colors. The nearest distance between the centerline of the structures is 7.5 voxels (between the mid points of the curves). Each curvilinear structure is generated through a convolution followed by a random sampling process described as in (Vasilkoski and Stepanyants, 2009). Traces of the curvilinear structures were convolved with a point spread function (PSF). Spherical Gaussian window with varying standard deviation, σ_{noise}, was used as

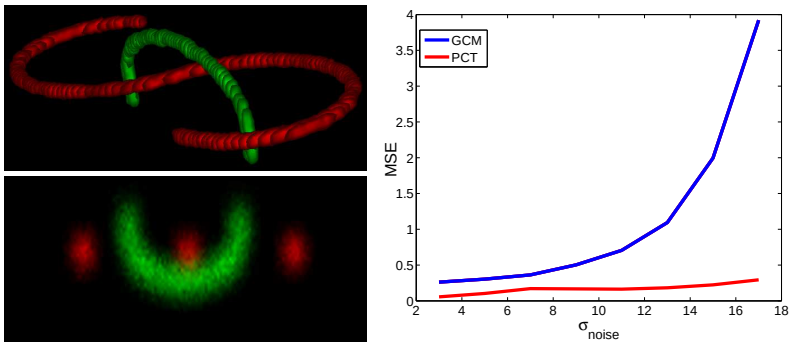

(a) (b)

Figure 4: (a) Top: 3D synthetic color data is generated through a convolution followed by a random sampling procedure. Bottom: Center yz slice. Increasing noise results in merging branches ($\sigma = 15$). (b) Average mean square error of the 50 Monte-Carlo simulations.

the PSF. In order to simulate the expected count of the photons at the receiver, we first linearly map the result of the convolution values to 0-100 range. Then, data samples were sampled from a Poisson density function having the mapped convolution result as the mean. Particular choice of the values are arbitrary to obtain a realistic synthetic data. By changing σ_{noise} of the convolving Gaussian function, we controlled the sample count observed around the underlying centerline. Red and green color channels were assigned with the sampling results to label distinct structures with different colors. Finally, data is obtained as the superposition of the curvilinear structures and the centerlines of branches are depicted in Fig. 4(a)-top using V3D software (Peng et al., 2010). As we increase the scale of the Gaussian function, σ_{noise}, curvilinear structures start to merge to each other due to the increasing noise level. Fig. 4(b)-bottom shows a yz cross section of the data where branches are merged to each other (Specifically, we used $\sigma_{noise} = 17$ for the Gaussian function). In our calculations, size of the Gaussian width that convolves the data is selected based on the "full width at half maximum" criteria and given as $2\sqrt{(2\ln(2))}\sigma_{noise}$, where ln is the natural logarithm. At each iteration, we traced the structure depicted with red color only. Fig. 4(b) presents the mean square error (MSE) of the PLCM and PCT algorithms. MSE is defined as the average squared deviation of the estimated centerline samples from the trace of the original curvilinear structure. PCT results in better centerline accuracy and more stable error profile and the error of PLCM algorithm increases as the noise level increases.

Described techniques were applied to Brainbow image set composed of 31 slices (z-direction resolution of 64 μm) with each slice being 1024×1024 pixels (x & y directions at 11 μm resolution). In the preprocessing step the images are downsampled by 3 in the x & y directions and upsampled by 2 in the z direction yielding a voxel size of $33 \times 33 \times 32$ μm^3. The resampled image stack is smoothed in 3D using a bilateral filter (Tomasi and Manduchi, 1998) using

a Gaussian kernel with diagonal covariance (spatial scale of 5 voxels and RGB-color scale of 0.2).

We applied the proposed algorithms on the Brainbow data. Algorithm performances are given in terms of qualitative and quantitative results. In order to obtain quantitative measures, we need ground-truth data which is not trivial to obtain especially for this particular dataset due to high concentration of fibers in compact small regions. Comparison with other methods is not possible because most of the methods in the literature assume highly sparse neuron distributions, or even operate on tracing of already segmented fibers and to the extent of our knowledge there is no segmentation or tracing algorithm for volumetric color images implemented before. Therefore, the comparison of algorithms is mainly with respect to the ground-truth labels obtained by manual tracing.

Since arbitrary cuts on cylindrical structures result in elliptical cross-sections (assuming cuts are not aligned with the fibers), in order to obtain the ground-truth data, we label fiber cross-sections in orthogonal slices (x-z plane) using ellipses. Although all fibers having sufficiently large intensity values (sufficient to observe when displayed without any complex enhancement method) in the dataset can be successfully traced with the proposed methods, we can not obtain ground-truth for some fibers using this strategy due to occlusions in 2D. For that reason reported quantitative results are obtained from fifteen fiber trajectories where ground-truth extraction procedure is not ambiguous, and fibers with corresponding edge maps can be clearly observed from the images. Obtained values from the algorithms and the ground-truth data are filtered using five-point moving average to get smoothed trajectories.

In order to emphasize weak edges, we also used the square-root of the edge values to select and iterate additional two fibers. Columns of Fig. 5 show a sample xz-plane slices of the brainbow image stack where (a) is the filtered image, (b) shows the corresponding edge map slices (enhanced to increase visibility), and (c) displays the selected fiber projections calculated using piecewise linear cylinder method (PLCM) on the square-root of the edge map.

Principal curve tracing algorithm (PCT) described here employs Gaussian kernels to estimate density. For simplicity, isotropic fixed bandwidth kernels are employed. We used an ϵ-ball having a radius sufficient to cover $N_x = 250$ neighbors (approximately radius of 4 voxels). Kernel covariances $\mathbf{\Sigma}_{i,p}$ and $\mathbf{\Sigma}_{i,c}$ are selected as $\sigma_p^2\mathbf{I}$ and $\sigma_c^2\mathbf{I}$ where $\sigma_p = 5$ and $\sigma_c = 0.3$. Since fiber colors vary along the axis, we employed moving averaging smoothing for the colors to adapt to this spatial color change along each axon. At each step, direction of the principal curve (ϑ_t) is calculated as described in Alg. 3. The immediate neighbor voxel center that is angularly closest to the direction pointed by ϑ_t is selected as the next approximate curve sample.

In order to obtain an accurate numerical comparison and to report the volume segmentation accuracy of the PLCM method, we applied the following procedure: for every image slice in the y-direction, we calculated the overlapping area between the algorithm cross-section (A1) obtained by a cut perpendicular to the local cylinder direction ($\mathbf{n}$) at the corresponding slice and the projection of the ground-truth ellipse (A2) to the cut plane defined by $\mathbf{n}$ at that slice.

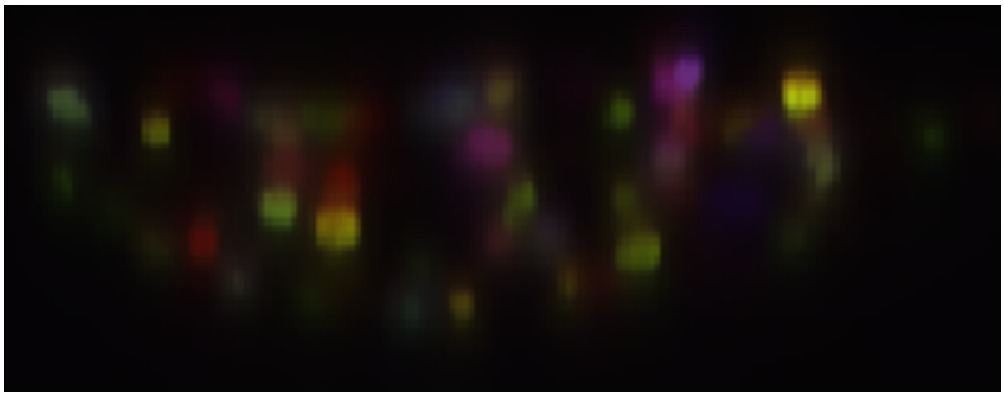

(a)

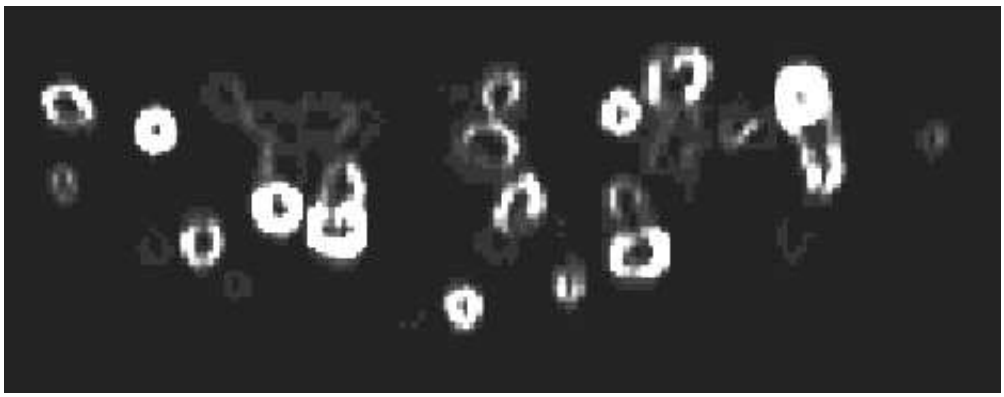

(b)

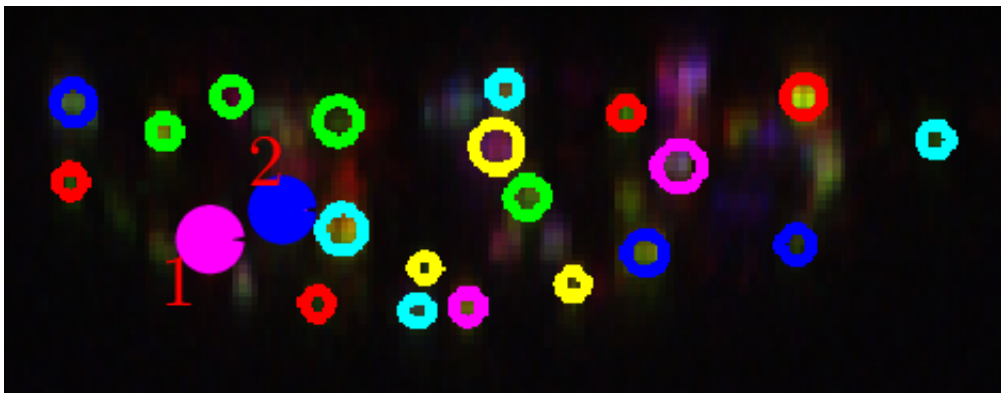

(c)

Figure 5: (a) A sample cross slice (yz-plane) of the Brainbow image stack. (b) Corresponding edge values. Edges are enhanced to increase visibility. (c) Fiber boundaries (PLCM) on the image slice showing the square-root of the edge values.

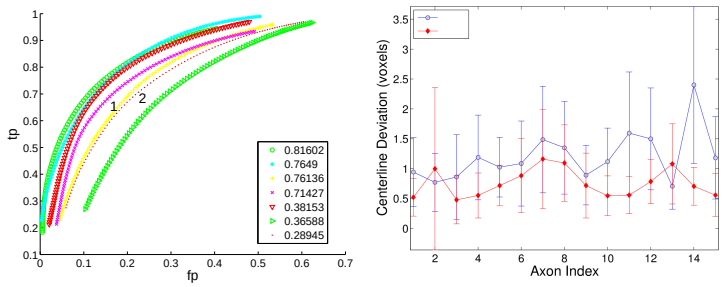

(a) (b)

Figure 6: (a)ROC curve for selected fibers. Legends are sorted by decreasing mean intensity along fibers. (b)Calculated centerline deviation of algorithm results. At $\alpha = 0.01$ significance level hypothesis stating means of PLCM and PCT, is rejected for all axons.

Since the cut is perpendicular to the cylinder direction, first cross-section is a circle having y-coordinate of it's center at the current slice. We approximated the projected ground-truth area as a circle centered at the mean of the projected voxel locations and containing all the projected voxel locations. Since estimated center might not coincide with the image slice, we used cubic spline interpolation to obtain the center locations. We also introduce a scale factor, that scales the radius of the estimated ground-truth projection. Obtained ROC curve can be seen in Fig. 6(a) for some selected traces. We define the area of the intersection of two circles (A1$\cap$A2) as true-positive (tp), area of relative complement of A2 in A1 (A1$\backslash$A2) as false positive (fp), and similarly area of the relative complement of A1 in A2 (A2$\backslash$A1) as true negative (tn). Each label in the figure indicates a mean of the intensity along a fiber trace obtained from the ground-truth. In general PLCM performs better as the intensity of a trace increases. Exceptions are the two neighboring fibers displayed with solid circles labeled with yellow and red colors and labeled with 1 and 2 at the bottom-left corner of Fig. 5-c, which are also labeled with yellow plus and red triangle in the ROC curve in Fig. 6(a) respectively. The reason is mainly interactions between fibers through calculated edge maps. The fiber represented with the red circle is relatively isolated and although it has a smaller intensity value along the trajectory, PLCM extracts its geometry better.

For each fiber, average displacement between the center of the projected ground-truth with the center of the algorithm outputs are displayed in Fig. 6(b). Error bars represent the standard deviation of error for each fiber trace. In general PCT outperforms PLCM in terms of deviation form the centerline, where overall average means for PLCM and PCT are 1.2068 voxels and 0.7565 voxels respectively. Here, one voxel is cubic with 33 μm side and the radius of a fiber is around 3 voxels ($100\mu m$).

4. Conclusion

The automatic identification and segmentation of fiber-shaped objects in 3D imagery is a commonly encountered problem. Brainbow images in particular provide a novel tool for neuroscientists to study the structure of the nervous system in vitro via confocal microscopy. In this paper, we presented two methods for identifying axons in 3D image sets using this modality.

PLCM: This approach uses edge and color information with weak shape priors incorporated in the form of a piecewise linear cylinder approximation and constraints imposed during the optimization process. The algorithm exploits the knowledge that each branch of an axon is a cylinder and approximates this form using piecewise linear cylinders locally. This approach eliminates the complicated global optimization required for active shapes or level sets that minimize energy functions over the whole volume or surface. The local cylinder fitting approach results in a relatively simpler energy minimization type problem and the piecewise approximation does not lose its ability to model complex axon trajectories. Continuity is guaranteed by imposing constraints on the search space for consecutive cylinder pieces and the final smooth cylinder can be approximated by a smooth interpolation technique such as cubic spline in 3D. While the algorithm utilizes the edge information to fit individual local cylinders, it employs color model continuity to prevent the local cylinders from jumping from one axon to another in the vicinity. In fitting the Gaussian color density model in uncorrelated RGB coordinates, we used the EM algorithm instead of sample mean and sample covariance estimates for the mean and covariance. It is possible for some voxels in the given cylinder or sphere to have a multimodal color distribution (e.g. background, target axon, and a neighbor axon with a different color), thus sample statistics will be severely influenced by these additional modes, which in turn could create problems in determining the local fiber direction using the largest eigenvector of the weighted covariance matrix during the tuning step or the length of the fiber that is calculated in the propagation step. Therefore propagation purely based on the edge values is not preferred and color values of the voxels are utilized. Problem formulation favors uniformly distributed strong edges having larger edge values which lead to easier segmentation of fibers. Depending on the location and the color, edge values vary throughout the dataset; thus proposed PLCM assumes a local thresholding strategy to adaptively select upper and lower bounds in the propagation step. Moreover, in order to emphasize the weak edges having smaller edge values, the square-root of the edge values are used. Choice of using the square-root of the edge values is heuristic and future work includes image enhancement strategies that will enable us to get more uniform edge value distributions throughout the dataset.

PCT: We also presented a curve tracing algorithm that uses locally defined critical set definitions. The proposed method uses the gradient and the Hessian of the density estimate to calculate the principal curves as the underlying structures. The computational complexity of PCT is $O(d^4N^2)$, where kernel density estimation requires $O(dN^3)$ and eigenvalue decomposition requires ad-

ditional $O(d^3)$. Here, N is the number of samples, and d is the dimension of the images ($d = 3$). While iterations on the constrained normal space pull towards to the principal curve, fixed step size or fixed-length updates trace the curve along the *center* of the data (if local maximum coincides with mean). Selection of the step size and kernel bandwidths are manual and proper selection should be determined by data geometry. Depending on the curvature, large step sizes might result in irrecoverable errors (one possible case in Brainbow analysis is two fibers with similar colors and high curvatures getting very close to each other - this might result in the traced curve to jump from one axon to the other). Kernel bandwidth selection is well researched for density estimation (e.g. leave-one-out cross validation maximum likelihood), but best density estimation bandwidth might not be the best principal curve estimation bandwidth and procedures specific to the latter should be researched in the future. Local principal set definition solves issues related to bifurcations, loops, and self intersections naturally. In tracing branching curves, one possibility is to initialize another tracing algorithm when a bifurcation is detected (indicated by a circular local Hessian on the curve). Algorithm highlights the centerline, so in order to obtain local geometry and the volume of fibers, region growing methods can be employed growing radially from the estimated centerline. Further work is needed to solve practical issues in this area.

The proposed approaches, at this point, aim to be semiautomatic in order to reduce the requirement of manual labor and intervention, yet allow the neuroscientist to have control over the identified axon-tree solutions. This will enable the accumulation of more ground-truth information about axon network geometries in various parts of the nervous system, thus will allow us to improve the presented algorithm in the future further by incorporating prior information that can be extracted from such a database. A desirable feature in semi-automatic segmentation is the ability of the user to intervene with the solution in a flexible and local manner. The proposed methods give the opportunity to the user to intervene in the initialization and during trace iterations while such interventions are not trivial to implement to the user's satisfaction in active shape or level set type approaches that seek global optimality.

Acknowledgment

EB and DE acknowledge support by the NSF grant IIS-0914808, BCS-1027724, IIS-1149570. The authors thank Dana Brooks and William Bosl for valuable discussions.

References

Al-Kofahi, K., Can, A., Lasek, S., Szarowski, D., Dowell-Mesfin, N., Shain, W., Turner, J., Roysam, B., Dec. 2003. Median-based robust algorithms for tracing neurons from noisy confocal microscope images. Information Technology in Biomedicine, IEEE Transactions on 7 (4), 302–317.

Al-Kofahi, K., Lasek, S., Szarowski, D., Pace, C., Nagy, G., Turner, J., Roysam, B., June 2002. Rapid automated three-dimensional tracing of neurons from confocal image stacks. Information Technology in Biomedicine, IEEE Transactions on 6 (2), 171–187.

Alley, R. E., 1996. Algorithm theoretical basis document for decorrelation stretch. Tech. rep.

Ascher, U., Petzold, L., 1998. Computer methods for ordinary differential equations and differential-algebraic equations. Society for Industrial Mathematics.

Ascoli, G., Donohue, D., Halavi, M., 2007. NeuroMorpho. Org: a central resource for neuronal morphologies. Journal of Neuroscience 27 (35), 9247.

Aykac, D., Hoffman, E., McLennan, G., Reinhardt, J., Aug. 2003. Segmentation and analysis of the human airway tree from three-dimensional x-ray ct images. Medical Imaging, IEEE Transactions on 22 (8), 940–950.

Bas, E., Erdogmus, D., April 2010a. Piecewise linear cylinder models for 3-dimensional axon segmentation. In: Biomedical Imaging: From Nano to Macro, 2010. ISBI 2010. 4th IEEE International Symposium on.

Bas, E., Erdogmus, D., April 2010b. Principal curve tracing. In: European Symposium on Artificial Neural Networks.

Bauer, R., January-February 2000. Distribution of points on a sphere with applications to star catalogs. Journal of Guidance, Control, and Dynamics.

Cai, H., Xu, X., Lu, J., Lichtman, J., Yung, S., Wong, S. T., 2006. Repulsive force based snake model to segment and track neuronal axons in 3d microscopy image stacks. Neuroimage 32, 1608–1620.

Cai, H., Xu, X., Lu, J., Lichtman, J., Yung, S., Wong, S. T., 2008. Using nonlinear diffusion and mean shift to detect and connect cross-sections of axons in 3d optical microscopy images. Medical Image Analysis 12 (6), 666 – 675, special issue on information processing in medical imaging 2007.

Cherkassky, B., Goldberg, A., Radzik, T., 1996. Shortest paths algorithms: theory and experimental evaluation. Mathematical programming 73 (2), 129–174.

Cohen, A. R., Roysam, B., Turner, J., 1994. Automated tracing and volume measurements of neurons from 3d confocal fluorescence microscopy data. Microscopy 173 (2), 103–114.

Comaniciu, D., Meer, P., 2002. Mean shift: A robust approach toward feature space analysis. Pattern Analysis and Machine Intelligence, IEEE Transactions on 24 (5), 603–619.

Cruz, A. L., Straka, M., Köchl, A., Srámek, M., Gröller, M. E., Fleischmann, D., 2004. Non-linear model fitting to parameterize diseased blood vessels. In: IEEE (Ed.), IEEE Visualization 2004. Institute of Computer Graphics and Algorithms, Vienna University of Technology, IEEE, pp. 400–393.

Dempster, A., Laird, N., Rubin, D., et al., 1977. Maximum likelihood from incomplete data via the EM algorithm. Journal of the Royal Statistical Society. Series B (Methodological) 39 (1), 1–38.

Deschamps, T., Cohen, L., Dec. 2001. Fast extraction of minimal paths in 3D images and applications to virtual endoscopy. Medical Image Analysis 5 (4).

Eberly, D., 1996. Ridges in image and data analysis. Kluwer Academic Pub.

Feng, G., Mellor, R. H., Bernstein, M., Keller-Peck, C., Nguyen, Q. T., Wallace, M., Nerbonne, J. M., Lichtman, J., Sanes, J. R., 2000. Imaging neuronal subsets in transgenic mice expressing multiple spectral variants of gfp. Neuron 28, 41–51.

Fletcher, R., Powell, M., 1963. A rapidly convergent descent method for minimization. The Computer Journal 6 (2), 163.

Frangi, A., Niessen, W., Hoogeveen, R., van Walsum, T., Viergever, M., October 1999. Model-based quantitation of 3-d magnetic resonance angiographic images 18 (10), 946–956.

González, G., Turetken, E., Fleuret, F., Fua, P., 2010. Delineating trees in noisy 2D images and 3D image-stacks. In: Computer Vision and Pattern Recognition (CVPR), 2010 IEEE Conference on. IEEE, pp. 2799–2806.

Hampel, S., Chung, P., McKellar, C., Hall, D., Looger, L., Simpson, J., 2011. Drosophila Brainbow: a recombinase-based fluorescence labeling technique to subdivide neural expression patterns. Nature Methods.

Hastie, T., Stuetzle, W., 1989. Principal curves. Journal of the American Statistical Association 84 (406), 502–516.

Kasthuri, N., Lichtman, J., 2003. The role of neuronal identity in synaptic competition. Nature 424, 426–430.

Kégl, B., Krzyzak, A., Linder, T., Zeger, K., 2002. Learning and design of principal curves. Pattern Analysis and Machine Intelligence, IEEE Transactions on 22 (3), 281–297.

Kitamura, K., Tobis, J., Sklansky, J., Sep 1988. Estimating the 3d skeletons and transverse areas of coronary arteries from biplane angiograms. Medical Imaging, IEEE Transactions on 7 (3), 173–187.

Lee, H.-C., Cok, D., May 1991. Detecting boundaries in a vector field. IEEE Trans. on Signal Processing 39 (5), 1181–1194.

Lee, T. C., Kashyap, R. L., Chu, C. N., November 1994. Building skeleton models via 3-d medial surface axis thinning algorithms. Graphical Models and Image Processing 56 (6), 462–478.
URL http://dx.doi.org/10.1006/cgip.1994.1042

Lesage, D., Angelini, E., Bloch, I., Funka-Lea, G., May 2008. Medial-based bayesian tracking for vascular segmentation: Application to coronary arteries in 3d ct angiography. In: Biomedical Imaging: From Nano to Macro, 2008. ISBI 2008. 5th IEEE International Symposium on. pp. 268–271.

Lichtman, J., Livet, J., Sanes, J., 2008. A technicolour approach to the connectome. Nature Reviews Neuroscience 9 (6), 417–422.

Livet, J., Weissman, T., Kang, H., Draft, R., Lu, J., Bennis, R., Sanes, J., Lichtman, J., 2007. Transgenic strategies for combinatorial expression of fluorescent proteins in the nervous system. Nature 450 (7166), 56–62.

Lu, J., 2011. Neuronal tracing for connectomic studies. Neuroinformatics 9 (2), 159–166.

Meijering, E., 2010. Neuron tracing in perspective. Cytometry Part A 77 (7), 693–704.

Meijering, E., Jacob, M., Sarria, J.-C., Steiner, P., Hirling, H., Unser, M., April 2004. Design and validation of a tool for neurite tracing and analysis in fluorescence microscopy images. Cytometry Part A 58A (2), 167–176.

Mikaël, R., Nikos, P., Rachid, D., Oct. 2003. Active shape models from a level set perspective. Tech. Rep. 4984, INRIA.
URL http://www-sop.inria.fr/rapports/sophia/RR-4984.html

Miller, J., 1998. Relative critical sets in RR (N) and applications to image analysis.

Nain, D., Yezzi, A., Turk, G., 2004. Vessel segmentation using a shape driven flow. In: in Proc. of MICCAI'04. pp. 51–59.

Osher, S., Sethian, J. A., 1988. Fronts propagating with curvature dependent speed: Algorithms based on hamilton-jacobi formulations. Journal of Computational Physics 79, 12–49.

Ozertem, U., 2008. Locally Defined Principal Curves and Surfaces. Ph.D. thesis, Oregon Health & Science University, Department of Science & Engineering.

Ozertem, U., Erdogmus, D., 2011. Locally defined principal curves and surfaces. Journal of Machine Learning Research 12, 1249–1286.

Palágyi, K., Kuba, A., 1998. A 3d 6-subiteration thinning algorithm for extracting medial lines. Pattern Recogn. Lett. 19 (7), 613–627.

Peng, H., Ruan, Z., Long, F., Simpson, J., Myers, E., 2010. V3D enables real-time 3D visualization and quantitative analysis of large-scale biological image data sets. Nature biotechnology.

Santamaría-Pang, A., Colbert, C., Saggau, P., Kakadiaris, I., 2007. Automatic centerline extraction of irregular tubular structures using probability volumes from multiphoton imaging. Medical Image Computing and Computer-Assisted Intervention–MICCAI 2007, 486–494.

Sato, Y., Nakajima, S., Shiraga, N., Atsumi, H., Yoshida, S., Koller, T., Gerig, G., Kikinis, R., 1998. 3d multi-scale line filter for segmentation and visualization of curvilinear structures in medical images. Medical Image Analysis, 143–168.

Schmitt, S., Scholz, M., Evers, J., Obermayer, K., Duch, K., 2004. New methods for the computer-assisted 3d reconstruction of neurons. NeuroImage 23, 1283–1298.

Silverman, B., 1998. Density estimation for statistics and data analysis. Chapman & Hall/CRC.

Streekstra, G., van Pelt, J., 2002. Analysis of tubular structures in three-dimensional confocal images. Network: Computation in Neural Systems 13 (3), 381–395.

Tomasi, C., Manduchi, R., 1998. Bilateral filtering for gray and color images. pp. 839–846.

Tyrrell, J. A., di Tomaso, E., Fuja, D., Tong, R., Kozak, K., Jain, R. K., Roysam, B., 2007. Robust 3-d modeling of vasculature imagery using superellipsoids. IEEE Trans. Med. Imaging 26 (2), 223–237.

Vasilkoski, Z., Stepanyants, A., 2009. Detection of the optimal neuron traces in confocal microscopy images. Journal of Neuroscience Methods 178 (1), 197 – 204.

Waltz, R., Morales, J., Nocedal, J., Orban, D., 2006. An interior algorithm for nonlinear optimization that combines line search and trust region steps. Mathematical Programming 107 (3), 391–408.

Wang, J., Zhou, X., Lu, J., Lichtman, J., Chang, S.-F., Wong, S., April 2007. Dynamic local tracing for 3d axon curvilinear strucutre detection from microscopic image stack. In: Biomedical Imaging: From Nano to Macro, 2007. ISBI 2007. 4th IEEE International Symposium on. pp. 81–84.

Wink, O., Niessen, W., Viergever, M., Jan. 2004. Multiscale vessel tracking. Medical Imaging, IEEE Transactions on 23 (1), 130–133.

Zhang, Y., Zhou, X., Lu, J., Lichtman, J., Adjeroh, D., Wong, S. T. C., 2008. 3d axon structure extraction and analysis in confocal fluorescence microscopy images. Neural Computation 20 (8), 1899–1927.

Zhou, W., Li, H., Zhou, X., 2008. 3d dendrite reconstruction and spine identification. In: Proc. of MICCAI '08, Part II. Springer-Verlag, Berlin, Heidelberg, pp. 18–26.

Zhu, X., Xue, Z., Gao, X., Zhu, Y., Wong, S. T., 2009. Voles: Vascularity-oriented level set algorithm for pulmonary vessel segmentation in image guided intervention therapy. In: Proc. of ISBI'09.